Article

Study on Discharge Characteristics and Microstructural Evolution of PEO Coatings Based on an Al/Ti Tracer Substrate

Guodong Li [1,2] , **Guang Li** [1,2] **and Yuan Xia** [1,2,*]

1   Institute of Mechanics, Chinese Academy of Sciences, Beijing 100190, China; lgd@imech.ac.cn (G.L.); lghit@imech.ac.cn (G.L.)
2   University of Chinese Academy of Sciences, Beijing 100049, China
*   Correspondence: xia@imech.ac.cn

Abstract: In this study, samples underwent plasma electrolytic oxidation (PEO) treatment using Al/Ti tracer substrates for 5, 10, 20, 35, and 55 min. The ionization states were determined using Optical Emission Spectroscopy (OES). Microstructural and elemental analyses were conducted using scanning electron microscopy equipped with energy dispersive spectrometry (SEM-EDS). The structural organization and phase composition of the coatings were characterized using X-ray diffraction (XRD) and Raman spectroscopy, respectively. The research findings indicate that the early discharge stage is dominated by discharge within the pre-deposited Al layer, which undergoes gradual oxidation along the thickness direction, while Ti (0.25 wt%) is found on the coating surface. The power increase was 56% of the total increase from min 5 to min 10 of discharge. As discharge time increased, the spectral peaks corresponding to Ti gradually became stronger and were accompanied by gradual enhancement of the crystallinity of the anatase and rutile phases within the coating. The coating surface displayed closed and semi-closed pores in the middle of the discharge. After 55 min of discharge, amorphous SiO_2 was observed and Ti content on the coating surface increased to 4.59 wt%.

Keywords: plasma electrolytic oxidation (PEO); optical emission spectroscopy; tracer substrate; evolution mechanism

1. Introduction

The plasma electrolytic oxidation (PEO) technique evolved from traditional anodic oxidation. It has a higher operating voltage accompanied by obvious plasma discharge at the anode, by which ceramic-like coatings can be in-situ-fabricated on valve metals (Al, Ti, Mg, etc.) and their alloys [1–6]. Metals such as Ti, Al, and their alloys are considered viable candidates for developing implantable materials in the medical field due to their satisfactory biocompatibilities. However, when these valve metals are exposed to corrosive physiological environments, coating techniques are required to create an oxide barrier layer on their surfaces [7]. Currently, methods such as the physical vapor deposition technique [8], cold spray technique [9], and ion beam-assisted deposition (IBAD) technique [10] can be employed to fabricate oxide coatings with high density and corrosion resistance. These methods also offer the advantage of being independent of substrate material limitations. However, under conditions of high flexural fatigue or strong corrosion, the abovementioned techniques require enhanced bond strength at the coating–substrate interface. PEO technique [11], which produces oxide coatings on the surfaces of valve metals through in situ reactions, demonstrates the distinct advantage of high adhesion strength. The in situ characteristics and inherent porous ceramic structure of PEO coatings amplify the diversity of their functions, including high wear resistance, corrosion resistance, and thermophysical properties [4–6]. Moreover, PEO has emerged as the most promising technique for the preparation of oxide films due to its advantages of low environmental pollution, high coating growth rate, and excellent reproducibility. However, the PEO

process is quite complex due to the involvement of thermal, chemical, electrochemical, and plasma oxidation reactions, which pose significant challenges to the study of discharge characteristics and coating growth mechanisms in PEO.

To investigate the growth mechanism of PEO, researchers have conducted extensive studies on the coating growth process by combining liquid-phase discharge model theory research with techniques such as plasma discharge monitoring in the past decade, enhancing our understanding of the growth of PEO coatings. Studies [12,13] have revealed that the growth of PEO coatings occurs through simultaneous inward and outward processes. In the early stage of the PEO process, the coating primarily grows inward from the metal substrate. During this process, the plasma discharge significantly influences the growth mechanism of PEO coatings. Alexander Sobolev [14] indicates that under low-frequency discharge, numerous type B discharges will occur, untimely, within PEO coatings in the middle of the discharge and become dominant as the discharge continues. As a result, the dense inner layer of the coating gradually evolves into numerous voids and non-uniform inner/outer layer interfaces. However, under high-frequency discharge, type A and type C discharges will occur mainly during the middle stage, with limited influence from type B discharges. This phenomenon persists until the late stage of the discharge, where the shockwave generated by type B discharges leads to the ejection of the molten oxide from the depth of the coating, which gradually evolves from a dual-layer structure to a typical "pancake" structure with several cavity defects. Although a series of studies [15,16] have been carried out on PEO coatings, the mechanisms underlying liquid-phase plasma discharge and coating evolution remain unclear. This is due to the bi-directionality of coating growth and the complexity of the discharge environment during the PEO process, making it difficult to directly capture the substrate's post-discharge motion and oxidation state within specific depth zones. Consequently, it heightens the difficulty of accurately analyzing the substrate–coating evolution behavior. To address this issue, our previous research [17] employed an Al/Ti tracer substrate to study the individual discharge channel of PEO coating and proposed a schematic model of the individual discharge channel based on trace analysis of the Ti element. Al/Ti tracer substrate is a layered structure made of two valve metals for the complex discharge reaction process of PEO. It can effectively monitor particle motion during PEO discharge, capturing dynamic processes during breakdown discharge; this is challenging with conventional substrates. Therefore, to further elaborate on the PEO discharge mechanism and coating evolution, this study uses Al/Ti tracer substrates to track particle motion during discharge.

To achieve better insights into the discharge process of PEO and the growth mechanism of the coatings, scholars have carried out extensive research on the discharge behavior of plasma during PEO of substrates such as Al [18,19], Ti [20,21], and Mg [22,23] using plasma emission spectroscopy technique. By analyzing the ion energy and composition of the discharged plasma, a variety of discharge models [24,25] have been improved. For example, Hussein et al. systematically studied the plasma discharge behavior during PEO processing of Al alloys using optical emission spectroscopy and proposed a PEO discharge model. Kasalica [26] employed OES to put forward a novel explanation for the growth patterns of nanoporous coatings and the evolution of irregular hemispherical objects (calottes) during PEO. Therefore, OES has emerged as a vital approach in recent research endeavors aimed at investigating micro-arc discharge and coating evolution mechanisms.

In light of the abovementioned situations, this research aims to investigate discharge characteristics and microstructural evolution during PEO processes using an Al/Ti tracer substrate. In this study, we employed the OES method to investigate the ionization state of the PEO process. To further confirm the trace element's trajectory, we utilized SEM and EDS to analyze the evolution mechanism of the coating's microstructure and discharge type. Additionally, XRD and Raman spectroscopy were employed to analyze the crystalline structure of the PEO coating at different stages and to analyze the internal correlations between plasma discharge characteristics, coating microstructure, and coating composition.

2. Materials and Methods

2.1. Preparation of Ceramic Coatings

As illustrated in Figure 1, the substrate used in this study consists of two components: a cylindrical substrate (Ti), which has a diameter of 38 mm and a thickness of 5 mm, and a layer of Al (~10 μm), which was pre-deposited on its surface using physical vapor deposition (PVD) technique to form an Al/Ti tracer substrate. The electrolyte consisted of Na_2SiO_3 (12 g/L), NaOH (2 g/L), and $Na_5P_3O_{10}$ (4 g/L), with EDTA (2 g/L) selected as a complexing agent. Prior to the experiment, the pre-weighed reagents were automatically stirred in deionized water for 10 min, and then the electrolyte was poured into the electrolytic cell. The chemical reagents were offered by Beijing Chemical Plant Co., LTD., China. The prepared electrolyte had a pH value of 11.4. The substrate was placed within a polytetrafluoroethylene (PTFE) fixture (Figure 1), which is enclosed on all sides but has an opening on the top. This arrangement ensured that the PEO discharge occurred solely on the surface of the substrate. The fixture contained internal connections for both the power supply and the substrate's conductive wires. An optical fiber probe was placed directly above the sample. During the experiment, the fixture containing the substrate was immersed in an electrolyte solution of Na_2SiO_3 series and connected to the anode of a WHD-30 direct current pulse power supply (constant voltage mode). The experimental equipment was independently developed by the Harbin Institute of Technology in China. The positive terminal of the power supply was linked to the fixture, while the negative terminal was connected to a terminal post on the electrolytic cell made of 304 stainless steel. The positive current density for all specimens was set to 0.12 A/cm^2, and the ratio of positive to negative current was 0.9:1. The duty cycle for positive and negative pulses was 50%, with a frequency of 1400 Hz. Our previous work [27] on discharged pure Al substrate indicated that closed pore structures were obtained during the later period of discharge at a current density of 0.12 A/cm^2 and a frequency of 1400 Hz. This phenomenon aligns with the desired microstructural structure for enhancing the thermal insulation property of coatings. Thus, the current study delves into the evolution of the patterns of the coating under these experimental parameters. Many researchers have categorized the PEO process into three [28,29] or four stages [12,30], with varying criteria based on discharge voltage or discharge condition. Prior to determining the time intervals in this study, we collected discharge voltages and OES spectra of PEO from 0 to 55 min. We observed a significant spark on the sample surface at 62 s, corresponding to the breakdown voltage [28] (Vb = 320 V); the voltage subsequently increased sharply. After 5 min of discharge, weak Ti II spectra were detected by OES. At 10 min, the increase rate of the voltage slowed noticeably (Figure 2) and numerous small arcs were observed on the sample surface, indicating entry into the near steady state [28]. After 20 min of discharge, the intensity of Ti II spectra began to increase gradually, with fewer arcs on the coating surface but increasing brightness. At 35 min, Ti II element content rose sharply again, with discharge voltage and arc discharge state stabilizing, indicating that the discharge entered the steady state [28]. After 55 min, concentrated discharge phenomena became exceptionally prominent, leading to the selection of 55 min as the experimental termination time. Considering the above analysis, this study identified 5 min, 10 min, 20 min, 35 min, and 55 min as the optimal time intervals. The fundamental electrical parameters of the experiments are summarized in Table 1.
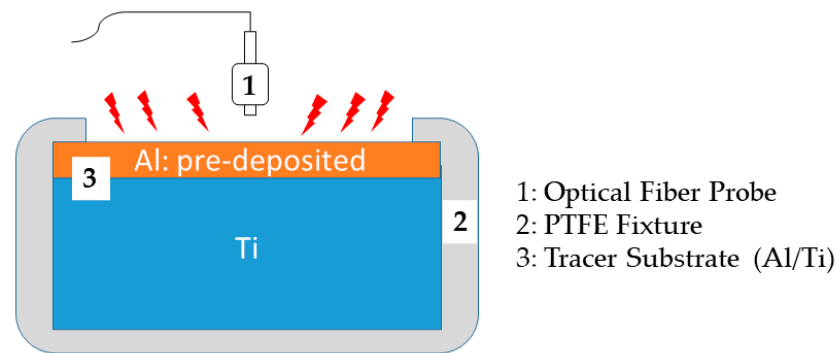
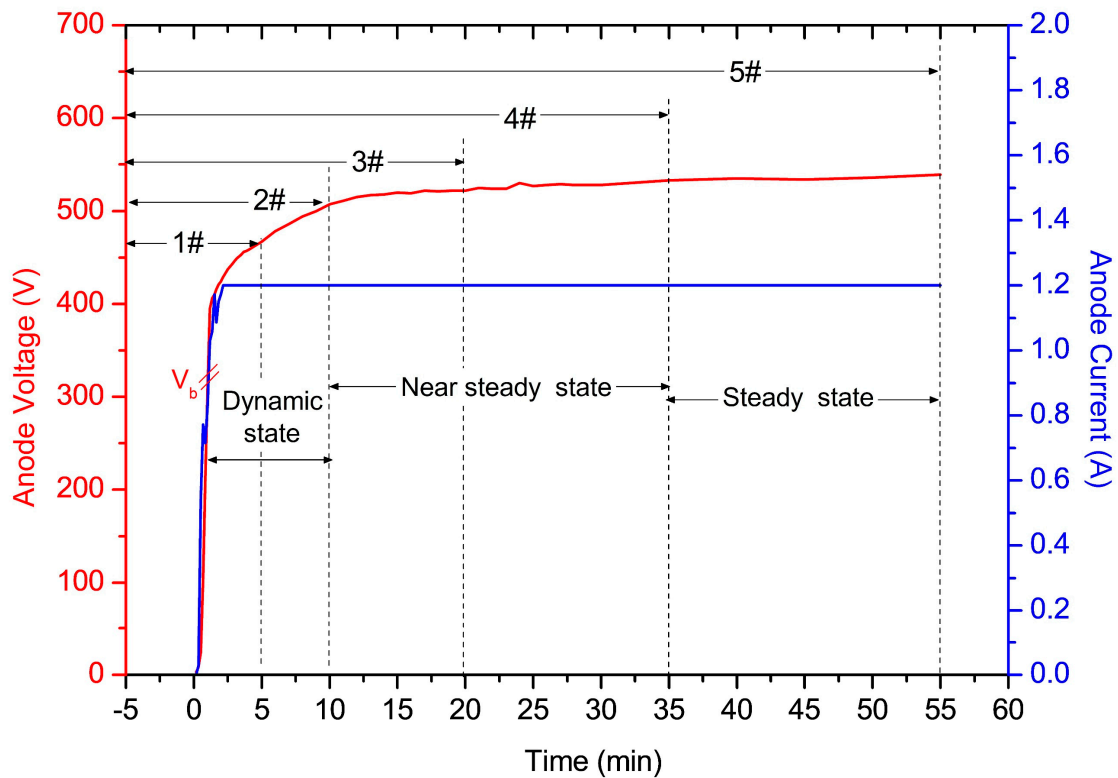**Figure 1.** Illustration of Al/Ti tracer substrate and its fixture equipment.

Figure 2. The relationship between PEO discharge time and anodic voltage/current.

Table 1. Technical parameters of the PEO process.

Sample No.	Substrate	Processing Time (min)	Frequency (Hz)	Current Ratio (+/−)	Duty Cycle
#1		5			
#2	Al/Ti	10			
#3	Al~10 μm	20	1400	0.9	50%/50%
#4	Ti~6 mm	35			
#5		55			

2.2. Characterization of the Ceramic Coatings

The surface morphology and elemental composition of the coatings were examined using a SUPRA55 scanning electron microscope (SEM, Oberkochen, German, Zeiss). X-ray diffractometry (XRD, Matsumoto, Japan, Rigaku-D/Max 2500) with CuKα radiation in grazing incidence mode (2°) was used. To further confirm the composition and structure of TiO_2, a Raman spectrometer (Raman, Paris, France, Horiba Scientific) with a resolution of

≤ 0.65 cm^{-1} was employed to detect the rutile and anatase phases within the coatings in the range of 100–900 cm^{-1}. Plasma spectrum data from PEO discharge were collected using an optical emission spectrometer (OES, Apeldoorn, The Netherlands, AvaSpec). Prior to data acquisition, the spectroscopic probe was positioned directly above the sample and the electrolytic cell was shielded using a black cover plate, with background light subtracted using signal acquisition software. During data collection, a four-channel monitoring mode was employed within a wavelength range of 200–1020 nm.

3. Results

3.1. PEO Discharge and Plasma Spectrum

Figure 2 depicts the relationship between current/voltage and sample time during the PEO process. The current rose quickly at 0–60 s but no plasma discharge was detected; this stage is attributed to anodic oxidation [28]. PEO power supplies with constant current mode output. At 120 s, the current increased to the set value (1.2 A) and then remained stable. It is evident from the graph that a rapid surge occurred in the anodic voltage within the initial 10 min, marking this period as the dynamic stage [31]. During this period, the sample surface exhibited a uniform distribution of numerous minute discharge sparks. In the 10–35 min time interval, the discharge sparks increasingly intensified, accompanied by a continuous increase in voltage. However, the rate of voltage ascent diminished, characterizing this phase as the near-steady state. After 35–55 min, the discharge phenomenon increased, with the voltage attaining a state of relative stability and exhibiting a negligible increase. This stage is denoted as the steady stage. In this stage, some regions on the sample surface tend to display concentrated discharge phenomena; these become increasingly pronounced as the discharge time increases. In this study, tracer samples obtained at typical time points during the aforementioned stages were selected as the subjects of investigation in subsequent analyses of coating evolution.

To further explore the discharge evolution of PEO, this study collected plasma emission spectral data at different time intervals. As depicted in Figure 3, the early stage of discharge exhibited prominent Al I double peaks (394.40 and 396.15 nm [18,19]). To confirm the ionization state of Al/Ti tracer samples over time more clearly, Figure 3b shows the comparison of the temporal evolution of the characteristic spectra corresponding to Al I and Ti II. As Figure 3b shows, the intensity of the Al I peak decreases rapidly as discharge time increases, reaching a significantly diminished state at 10 min of discharge. This suggests that for the Al/Ti tracer sample, the majority of the surface Al layer participates in the reaction within the initial 10 min. Conversely, the Ti II spectral peak displayed an increasing trend with increasing discharge time. Additionally, Figure 3a reveals the presence of Na I peaks (588.99, 589.89, and 819.47 nm [32,33]). The Na element originates from the electrolyte and the intensity of the Na spectrum reflects the degree of involvement of the electrolyte in the discharge reaction. It is evident from the Figure that the intensity of the Na peak continues to rise as the discharge time increases.

After 10 min of discharge, new spectral peaks corresponding to Ti I and Ti II were observed in the 292–430 nm wavelength range (Figure 3b); however, their intensities were relatively weak. XRD and Raman spectroscopy were used to analyze the coatings to further confirm the involvement of Ti elements at different times.
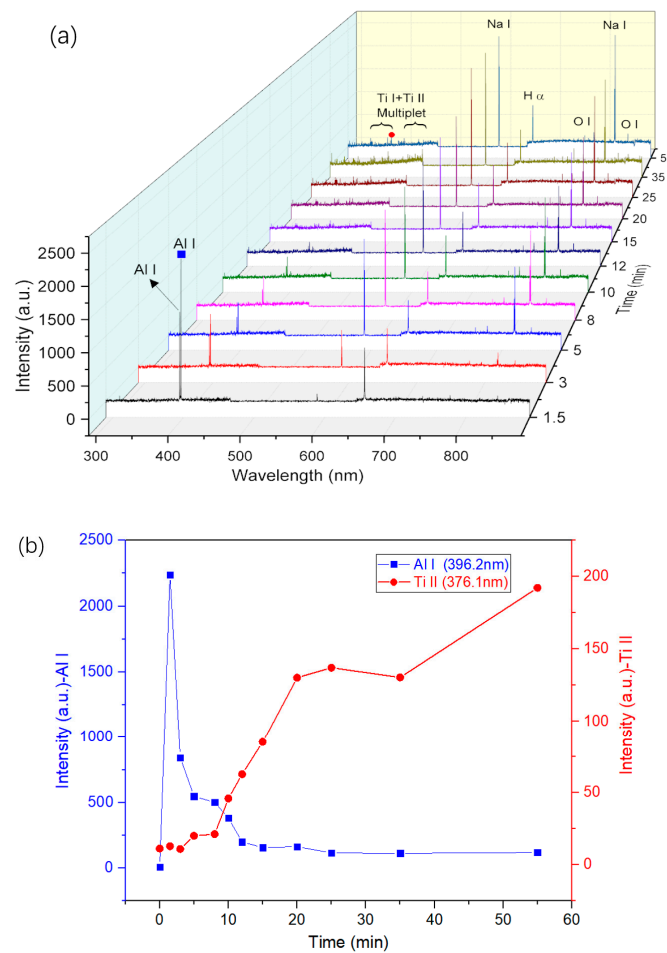
Figure 3. (**a**) Temporal evolution of plasma emission spectroscopy (1.5–55 min); (**b**) Temporal evolution of characteristic spectra corresponding to Al I and Ti II.

3.2. Morphology of PEO Coating

To explore the microstructural changes in PEO coatings and discharge types at various stages of discharge, the surface morphologies of the coatings at 5–55 min discharge times were compared. Hussain et al. [24] categorized discharges during the PEO process into three types: Type A discharge occurs on the surface of PEO coatings. Type B refers to strong discharges between PEO coatings and the substrate surface. During this process, a number of molten oxides eject instantaneously from the discharge channels, forming a relatively large "pancake" structure on the surface of the coatings [22]. Type C discharge occurs under PEO coatings. As illustrated in Figure 4, obvious and regular changes in the surface morphology were observed as discharge time increased. The changes in coating surface porosity and pore size are caused by voltage variations. In the early stage of discharge, low discharge voltage leads to the formation of compact coatings and small, dense micro-pores on the surface, with type A and type C discharges being predominantly observed. The pore sizes on the coating surface gradually increased during the intermediate and late stages of discharge, accompanied by an increase in the number of large pores. The results are consistent with research conducted by Fatemeh Salahshouri et al. [7]. Based on pore morphology, the larger pores can be classified into two: open-type pores induced by penetrating discharges, and "pancake" structured closed pores filled with re-discharged molten material (Figure 4(5)). The mechanism of its formation will be described in the Discussion section. Composite discharge structures were also detected within the pores (Figure 4(4,5)), indicating the involvement of type A and type C discharges alongside the dominant type B discharge during the formation of closed pores.
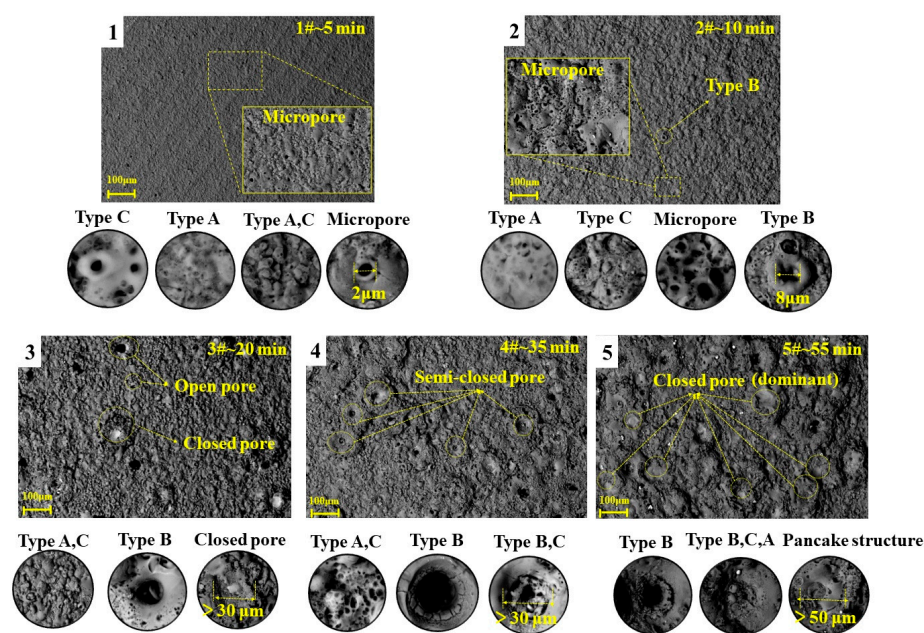
Figure 4. The temporal evolution of the morphology of PEO coating surface. (**1**) Sample after 5 min of PEO treatment, (**2**) sample after 10 min of PEO treatment, (**3**) sample after 20 min of PEO treatment, (**4**) sample after 35 min of PEO treatment, (**5**) sample after 55 min of PEO treatment.

To further investigate the mechanisms of evolution of the microstructure of PEO coatings, the cross-sectional morphology and elemental composition of tracer samples taken at different stages of PEO discharge were analyzed. As shown in Figure 5a, regular changes in coating structure and thickness were observed with increasing discharge times. As observed from the Ti element distribution map, the resolution of Ti element distribution in the coating was relatively low. This can be explained by the strong signal of Ti elements in the substrate, which weakens the resolution of Ti elements within the coating and has nothing to do with the Ti content in the coating. The temporal evolution of Al element distribution indicates that the Al layer on the surface was gradually oxidized and consumed during the initial 35 min of discharge, and the remaining Al layer almost completely disappeared in the 35th min of discharge.

Unexpectedly, we discovered the presence of Ti elements in the coating cross-section during the early stage of the discharge. However, it remains uncertain whether these penetrating discharges occur at the coating–substrate interface or if they penetrate deeper than the depth of the oxide layer; further experiments and investigations are required to determine these. Comparison of the elemental distribution across the cross-section of the coatings during the late discharge stage (35–55 min) demonstrates the appearance of large penetrating discharge channels through which numerous Ti eject beneath the coating. The ejection region of such discharge channels is predominantly characterized by Ti and its oxides derived from the substrate, with minimal presence of Al elements and their oxides. These findings are consistent with our previous investigation [17]. Figure 5a illustrates the elemental content of the coating cross-section where Ti content appears unusually high; this is attributed to matrix signal interference and coating non-uniformity. For a more precise depiction of individual element intensities within the coating, surface elemental composition analysis was conducted (Figure 5b). The figure reveals that Al content decreases to a stable range (reduced from 24.40 wt.% to 18.26 wt.%) after 20 min of discharge, and Ti element shows a clear increasing trend from 10 min (0.15 wt.%) to 55 min (4.59 wt.%) of discharge, consistent with OES detection data (Figure 3). This further corroborates that the involvement of Al in the discharge remains stable as the discharge time increases, while an increasing proportion of Ti from the substrate participates in the reaction during the late discharge stage.
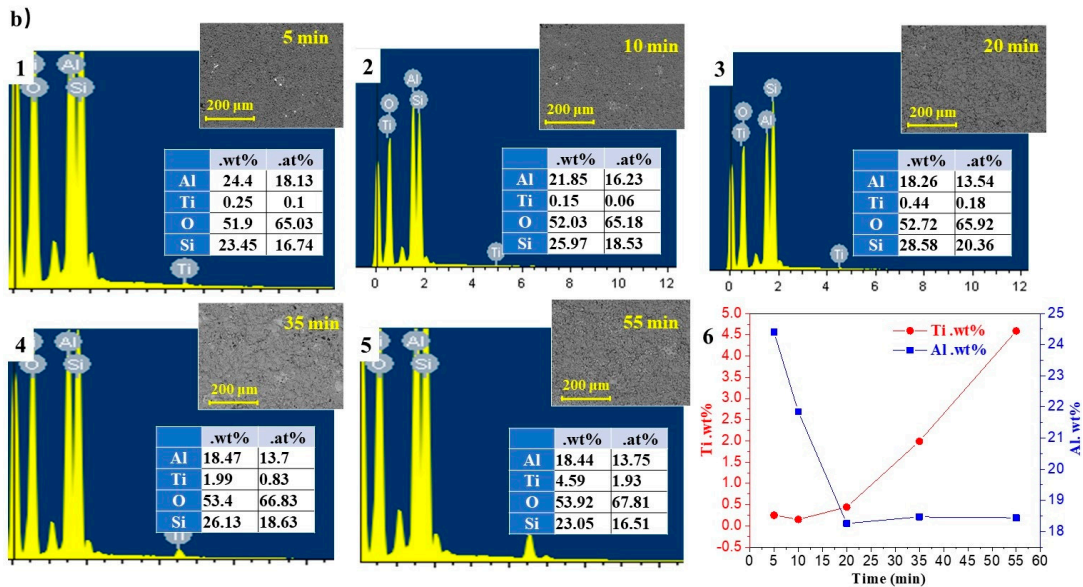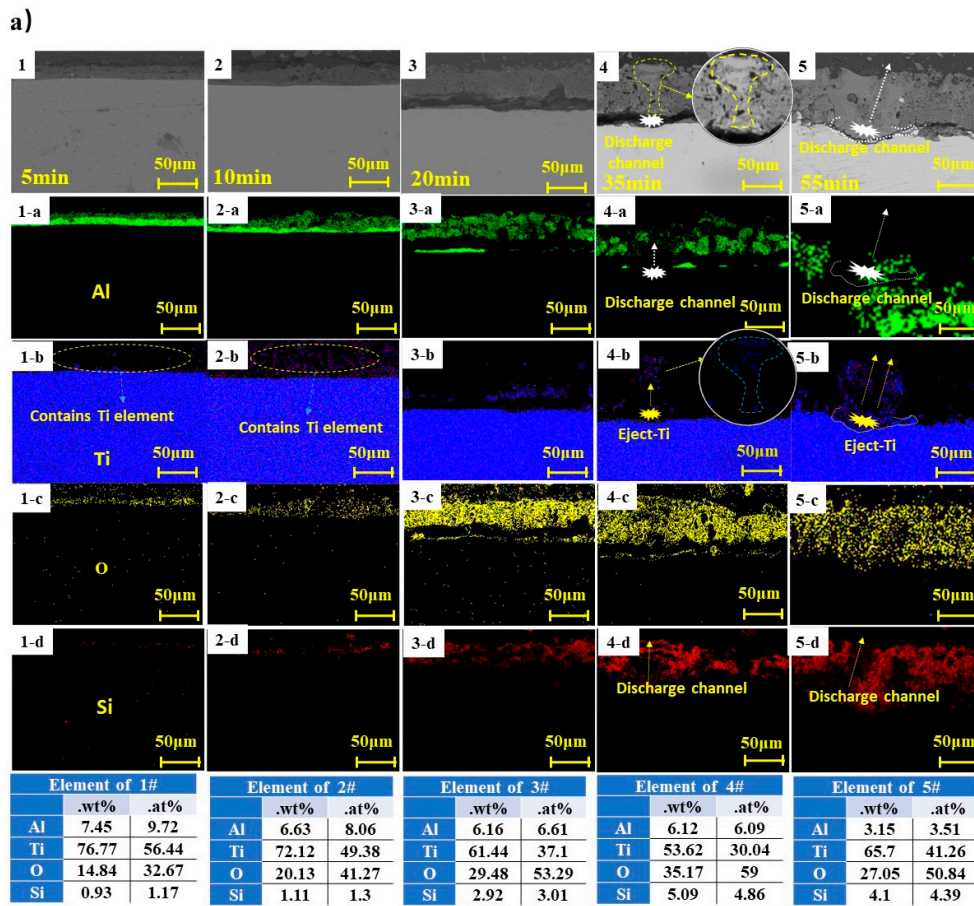
Figure 5. (**a**) PEO coating fracture morphology of trace substrate and element mapping evolution, "x-a", "x-b", "x-c" and "x-d" represent the distribution maps of the elements Al, Ti, O and Si for sample x, respectively. (**b**) elemental composition of coated surfaces. In both (**a**,**b**), 1 represents the sample after 5 min of PEO treatment, 2 represents the sample after 10 min of PEO treatment, 3 represents the sample after 20 min of PEO treatment, 4 represents the sample after 35 min of PEO treatment, and 5 represents the sample after 55 min of PEO treatment. In (**b**), 6 illustrates the variation of the content of elemental Al and Ti on the surface of each specimen as a function of time.

3.3. Phase Structure of PEO Coatings

The XRD patterns of the PEO coatings obtained at various discharge stages are shown in Figure 6a. As shown, the coatings are primarily composed of Al, Ti, anatase (A), rutile [®], γ-Al$_2$O$_3$, and α-Al$_2$O$_3$. The mullite phase was also detected.
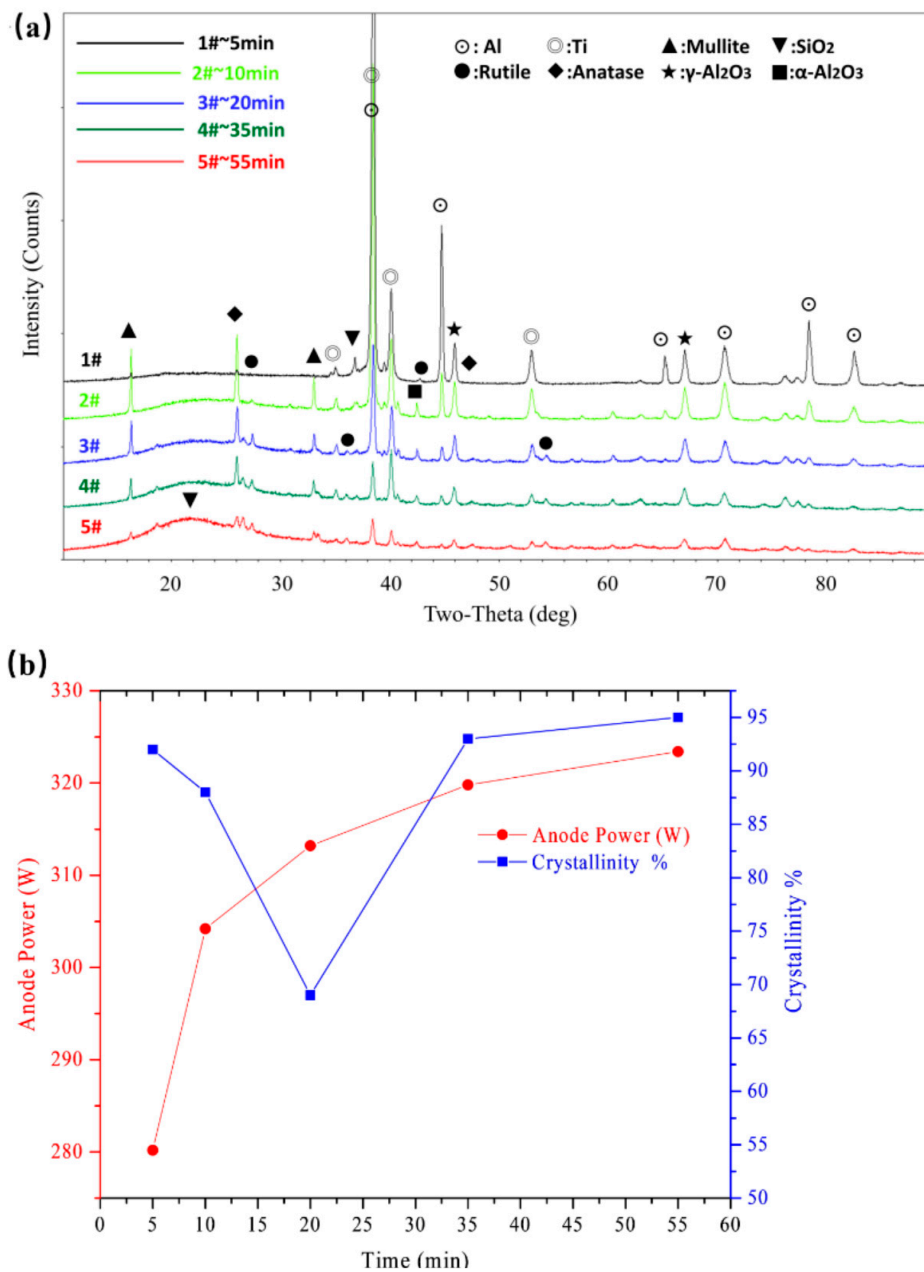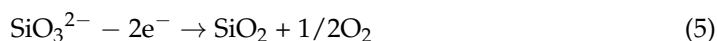

Figure 6. (**a**) XRD patterns at different discharge stages, (**b**) Correlation between coating crystallinity and discharge power at different discharge times.

Al$_2$O$_3$ reactions during the PEO process are shown in [2,12,34]:

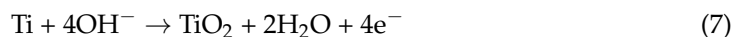$$Al \rightarrow Al^{3+} + 3e^- \tag{1}$$

$$Al^{3+} + 3OH^- \rightarrow Al(OH)_3 \tag{2}$$

$$2Al^{3+}\ 3O^{2-} \rightarrow Al_2O_3 \tag{3}$$

The reactions for generating the mullite phase are illustrated below:

$$Na_2SiO_3 \rightarrow 2Na^+ + SiO_3{}^{2-} \tag{4}$$

$$SiO_3{}^{2-} - 2e^- \rightarrow SiO_2 + 1/2O_2 \tag{5}$$

$$3Al_2O_3 + 2SiO_2 \rightarrow 3Al_2O_3 \cdot 2SiO_2 \tag{6}$$

The anodic reaction for Ti during the PEO process is illustrated below:

$$Ti + 4OH^- \rightarrow TiO_2 + 2H_2O + 4e^- \tag{7}$$

As the figures show, during the initial stage of discharge (5–10 min), intense diffraction peaks of both Al and Ti elements are detected. However, with prolonged discharge time (20–55 min), the diffraction peaks of Al gradually weaken (at 65.133°), while the Ti diffraction peak remains significant. This is attributed to the fact that during the initial stage of discharge, both Al and Ti originate from the Al/Ti layered structure of the substrate. As the discharge time increases, the Al on the coating surface is continuously oxidized until it is depleted, leaving only the Ti material in the substrate. With the progression of micro-arc oxidation and the increase in coating thickness, the diffraction peaks exhibit a decreasing trend, but the Ti substrate diffraction peaks can still be detected. This variation aligns with the results of microscopic morphology analysis. From Figure 6, it can be noted that Al is gradually consumed while a large amount of Ti and its oxides are ejected from the underlying layers, leading to the formation of the "pancake" structured closed holes on the coating surface.

Figure 6 shows that during the early stage of discharge, the coating exhibits an intense γ-Al_2O_3 phase that gradually weakens as the discharge time increases. Similarly, with prolonged discharge time, the amorphization degree of the SiO_2 phase within the coatings increases; this will be examined further in the Discussion section on EDS results and plasma spectroscopy data.

Additionally, Figure 6 shows the presence of rutile phase (R) and anatase phase (A) of TiO_2 after 10 min of PEO treatment, whereas no crystalline phase of TiO_2 was detected in the samples subjected to PEO treatment for 5 min. This is because Al discharge on the outermost layer of the substrate plays a dominant role in the early stage of discharge, with little involvement of the underlying Ti. However, as time passes, the discharge becomes more intense, leading to the emergence of penetrating discharge and internal coating discharge phenomena. Consequently, an increasing amount of Ti from the substrate gets involved in the reaction, resulting in the formation of rutile and anatase phases under high-temperature and high-pressure conditions.

Figure 6b illustrates the correlation between coating crystallinity and discharge power at different discharge times. The figure reveals that coating crystallinity is comparatively higher in the early and late stages of discharge, while discharge power continuously increases with prolonged discharge time. The power rose by a total of 43 W from 5 min to 55 min, with the most notable increase occurring during the early stage of discharge. The power increase from 5 min to 10 min of discharge accounted for 56% of the overall increment. In the late stages of discharge, the power only increased by 4 watts.

To further compare the composition and evolution patterns of the TiO_2 phases at various discharge stages, this investigation used Raman spectra to analyze selected samples. Figure 7 depicts the characterization of various tracer samples using Raman spectroscopy. As the graph shows, the Eg [35,36] vibrational mode of the anatase phase is observed at 141 cm^{-1}, and the Eg and A1g vibrational modes of rutile are detected at 445 cm^{-1} and 613 cm^{-1}, respectively. Additionally, a multiple scattering mode of rutile appears at 240 cm^{-1}. Weak and broad peaks were observed during the initial stages of discharge, indicating the composition of a certain amount of TiO_2 crystalline phase in the coating.

However, the crystallinity of TiO_2 was weak and the content was relatively low, consistent with findings from the XRD analysis.
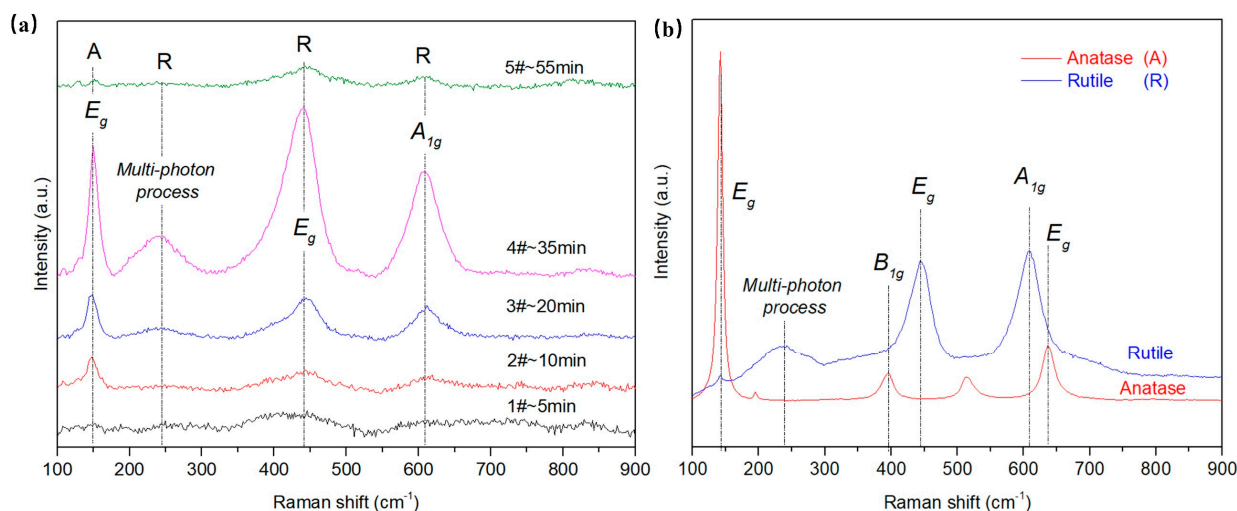
Figure 7. (**a**) Raman spectra measured at different discharge stages; (**b**) Raman spectra of the standard TiO_2-rutile (R) and TiO_2-anatase (A).

Significant vibrational modes associated with the anatase phase appeared within the coating when the discharge time reached 10 min. As the discharge time approached 20 min, the intensity of the anatase diffraction peak continued to increase and vibrational modes corresponding to the rutile phase were observed. With a further increase of the discharge time to 35 min, the Raman peak of the rutile phase gradually intensified, surpassing the intensity of the anatase phase. Finally, the anatase phase of the Raman peak nearly vanished at the 55th min of discharge.

4. Discussion

The aforementioned data demonstrates that the Al/Ti tracer samples exhibit regular changes in the patterns of plasma discharge characteristics, microstructural morphology, crystal structure, and plasma discharge behavior with increasing discharge time. In the following discussion, we will focus on the discharge characteristics and coating evolution mechanisms of the Al/Ti tracer samples during different time intervals.

The distribution of elements (Figure 5) and the plasma emission spectroscopy (Figure 3) indicate that a substantial amount of Al is involved in the reactions during the early stage of discharge of the Al/Ti-structured tracer substrate. From a macroscopic perspective, the Al layer is gradually consumed by oxidation along the thickness direction; this is predominantly attributed to the type A discharge on the surface of the PEO coating and the type C discharge beneath the oxide film. In addition, the Ti beneath the Al layer also participates in discharge reactions, although at a very low intensity. Combined with the results of plasma spectroscopic analysis, it is evident that the emission spectrum of Al during this stage is significantly strong. However, as the discharge time increases, the intensity of Al I emission gradually weakens, becoming extremely faint after approximately 10 min. Nevertheless, no spectral peak corresponding to Ti was detected during the initial discharge stage. Based on research by Stojadinovic [21,22] and the detection data from the experiment, the absence of a Ti spectrum peak does not imply the absence of Ti elements in the discharge. In addition, the anatase phase was found in the early stage of the discharge. Based on the literature [37], the peak of the anatase phase occurs at a temperature above 400 °C, indicating that the partial temperatures within the coating reached over 400 °C at that time.

For validation, EDS analysis was performed on the trace sample after 5 min of discharge, as shown in Figure 8, confirming the presence of tracer element Ti (blue) on the

surface of the coating. This, combined with the evolution pattern of Al elements, suggests that although type A and type C discharges are dominant on the surface Al layer during the early stage of the discharge, a small amount of penetrating discharge is involved in this stage. As a result, Ti elements beneath the coating are expelled to the coating surface through small penetrating discharge channels. This result is consistent with the Raman spectroscopy and XRD analyses conducted in this study.
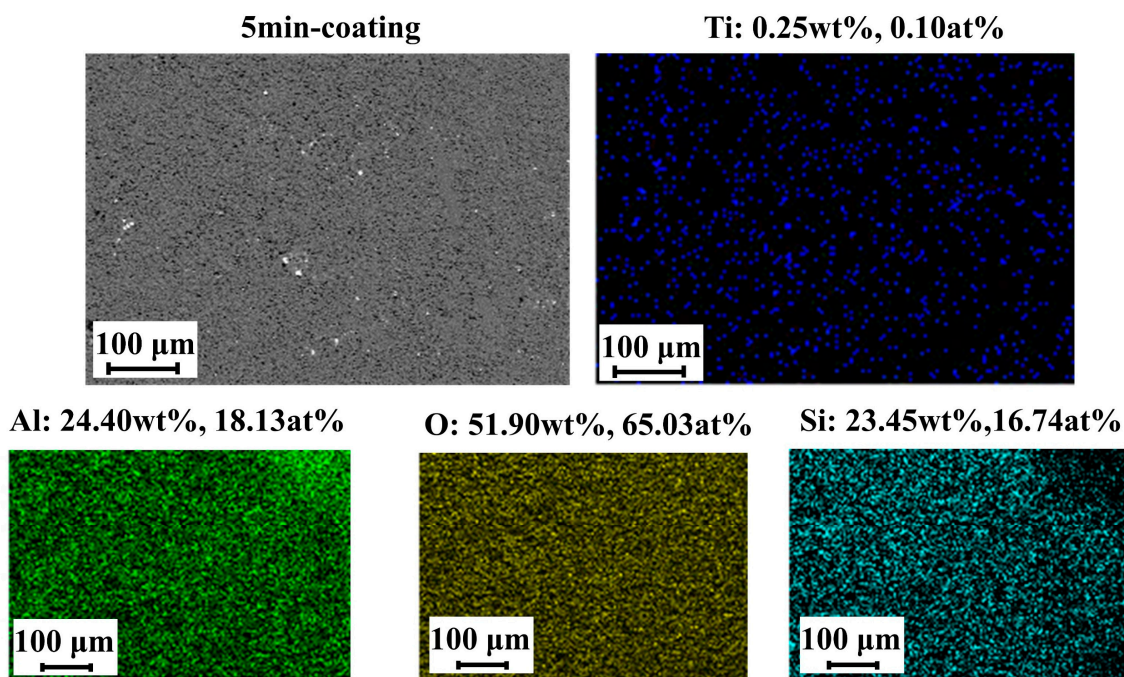
Figure 8. Distribution of Ti, Al, O, and Si elements on the surface of the tracer sample after 5 min of discharge, showing the existence of trace element Ti.

In the middle stage of the discharge, an increasing proportion of Al was gradually oxidized due to its involvement in the reactions. As a result, the α-Al_2O_3 phase formed within the coating. This can be explained by the fact that the critical nucleation-free energy of the α-Al_2O_3 phase is significantly higher than that of the γ-Al_2O_3. Moreover, at the dynamic stage, a lower discharge voltage (Figure 2) cannot provide sufficient energy for the transformation of Al_2O_3 into the stable phase, resulting in the preferential formation of γ-Al_2O_3 within the coating. However, as discharge voltage and energy increase, the discharge temperature of the partial region gradually rises, leading to the appearance of α-Al_2O_3 within the coating. This finding is consistent with the results of our previous research [27]. The anatase phase was observed in the 20th min of discharge, indicating that the partial temperature within the coating had increased above 700 °C. The crystallinity of the rutile TiO_2 phase and the rutile phase gradually increased with prolonged discharge time. This can be explained by the fact that as both discharge energy and partial temperature increase, an increasing proportion of the anatase phase is converted into the stable rutile phase.

Based on the research by Stojadinovic [21,22], the limited intensity of Ti spectra during PEO discharge can be attributed to two factors: the relatively high melting point of Ti and the composition of the electrolyte. Therefore, the appearance of new Ti I and Ti II peaks in the late discharge period (Figure 3b) signifies a pronounced discharge phenomenon involving Ti. Moreover, as time passed, the proportion of the rutile phase progressively increased. Furthermore, it was observed that the size of the pore structures on the surface coating increased compared with the size of the pores in the early stage of discharge. This phenomenon can be primarily attributed to the fact that the discharge power was relatively low during the initial discharge (Figure 6b), with discharges mainly taking the form of type A and type C discharges. As the thickness of the coating continued to increase, the

discharge power also increased (from 280 W to 323 W). This high-energy discharge tended to occur persistently in regions of the coating with relatively lower strength, leading to an increase in pore size. This phase is predominantly characterized by type B discharges. This observed phenomenon aligns well with the findings of Elinor Zadkani Nahum et al.'s research [11]. Based on their morphology, these large pores can be classified into two types: open-type pores induced by penetrating discharges and closed pores filled with molten material. The latter is attributed to the occurrence of concentrated discharges at the coating–substrate interface.

Following the formation of open pores, breakdown discharges continued to occur between the electrolyte inside the pores and the substrate (Figure 9(1-b)). Consequently, a significant amount of high-temperature plasma was generated within the discharge region. These hot gases carry molten metal substrate and oxides, which are rapidly expelled and quickly accumulate in the open pores upon encountering cooler electrolytes. As these expelled materials continued to accumulate (Figure 9(3)), "pancake" structured closed pores eventually formed near the pore opening. Moreover, as depicted in Figure 9(2), compound discharges occurred within the accumulated materials, resulting in the formation of small "honeycomb" structured pores within the accumulation, giving rise to semi-closed pores featuring large-sized pores encompassing small "honeycomb" structured pores. Alexander et al. [14] also observed this phenomenon, which is attributed to the sustained concentrated discharge occurring in certain areas during the late stage of discharge. At this stage, type B discharges pass through the entire depth of the coating, generating shock waves that lead to plasma expansion. This is followed by charged gases carrying molten metal substrate and oxides, which are expelled outward. Upon encountering the cooler electrolyte, the reaction products rapidly solidify and accumulate at the discharge channel's opening, thus forming a typical "pancake" structure. The observations in Figure 4(5) and Figure 9 align well with Alexander's analysis and clearly illustrate the process of evolution of these closed pore structures.
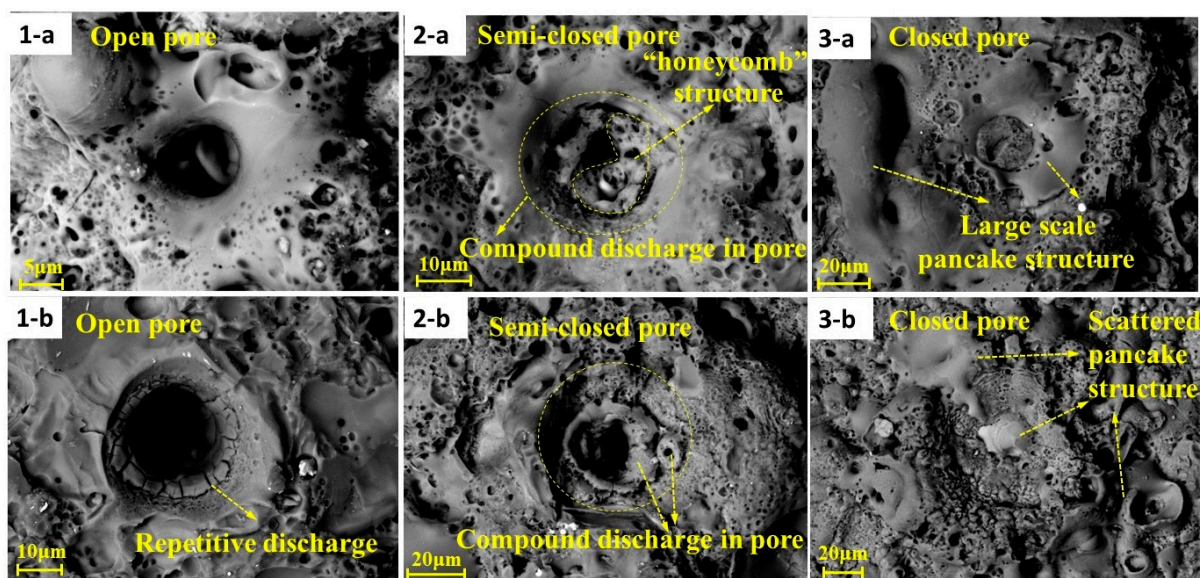
Figure 9. Pore morphology and discharge forms. (**1-a**) open pore, (**1-b**) open pore with repetitive discharge, (**2-a**) "honeycomb" structured semi-closed pores induced by compound discharge within pores, (**2-b**) semi-closed pores induced by compound discharge within pores, (**3-a**) closed pores and large scale "pancake" structure, (**3-b**) closed pores and scattered "pancake" structure.

Partial discharge becomes particularly pronounced during the late stage of discharge and is accompanied by increasing quantities of "pancake" structured closed pores. As the plasma spectroscopy data shows, more Ti was involved in the reaction at this stage and the discharge at the coating–substrate interface became particularly obvious; this was followed

by the increasingly prominent Ti plasma spectroscopy signal. To further substantiate the conclusion that pore structures originate from the Ti substrate in the late discharge stage, elemental distribution analysis of the pore structures was performed, as shown in Figure 10. It is evident from the Figure that the Ti elements are predominantly distributed around the discharge pore region, with lower predominance elsewhere, consistent with the findings of the plasma spectroscopic analysis. Additionally, brighter green regions (Si) can be observed within pores, indicating the increased participation of SiO_3^{2-} from the electrolyte in the high-energy discharge reactions occurring within the large penetrating pores. The higher temperature in the vicinity of the pores facilitates the formation of amorphous SiO_2, which explains the subsequent discovery of a significant peak corresponding to amorphous SiO_2 in the XRD analysis. Moreover, due to the predominance of high-energy penetrating discharges at this stage, the TiO_2 within the coating exists mainly in the rutile phase, while the metastable anatase phase is negligible, indicating that the principal composition of crystalline TiO_2 within the coating had evolved into the rutile phase.
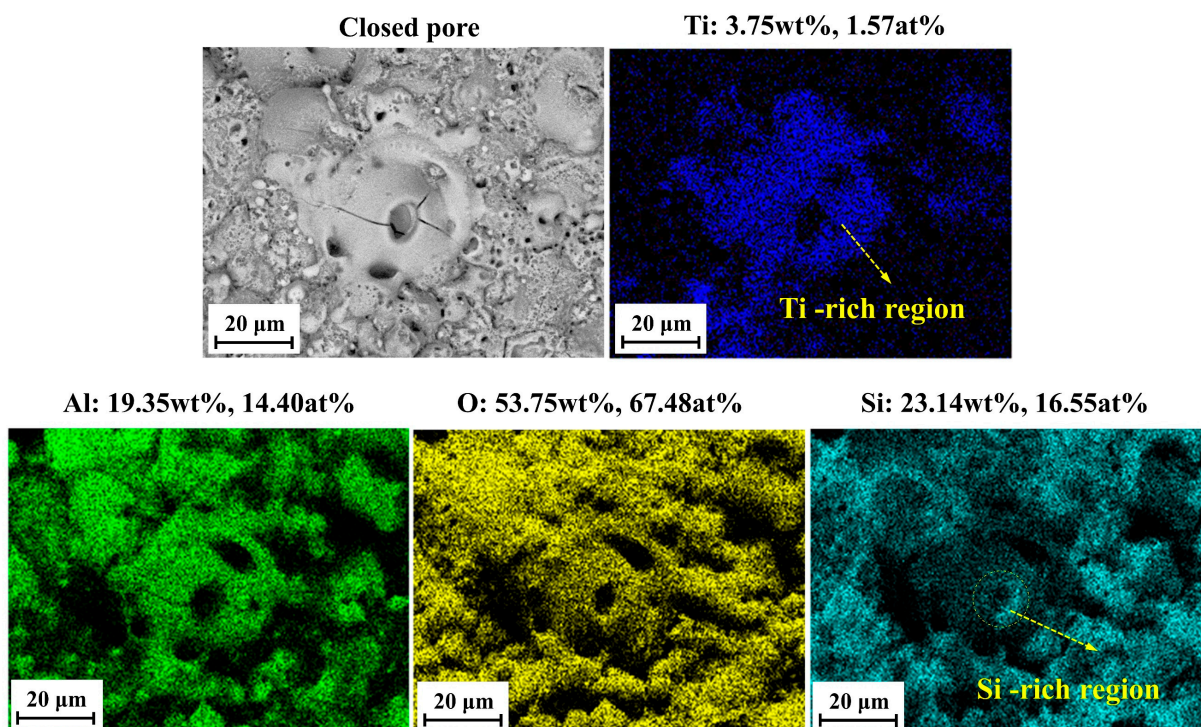

Figure 10. Element distribution in the closed pore region.

5. Conclusions

We studied the discharge characteristics and microstructure evolution of plasma electrolytic oxidation (PEO) at various stages (5–55 min). The following conclusions were drawn:

(1) Regarding the Al/Ti tracer sample, during the initial non-steady-state stage of the discharge, the primary discharge reaction occurs on the surface of the Al layer. However, as time passes, the surface coating undergoes gradual oxidation along the thickness direction, resulting in the formation of small micro-pores on the coating surface. Unexpectedly, the Ti substrate also participates in the discharge, although the crystallinity of TiO_2 at this stage is relatively low.

(2) In the middle stage of the discharge, the PEO process enters a near steady-state phase where the intensity of the plasma spectrum gradually increases. At this stage, the Al peak becomes undetectable, while new peaks corresponding to Ti I and Ti II appear. A significant number of porous structures occur on the coating surface and the intensity of type B discharges at the coating–substrate interface intensifies, indicating substan-

tial Ti involvement in this process. Due to the higher discharge energy involved in this stage, the proportion of anatase phase TiO_2 gradually decreases while the proportion of rutile phase TiO_2 gradually increases. This trend continues until the late stage of the discharge when the majority of TiO_2 evolves into a rutile-phase structure.

(3) During the late stage of discharge, an increasing amount of Ti participates in discharge reactions at the membrane interface. Based on the results of elemental analysis, the enrichment zone of Ti is primarily in the vicinity of the large pore structures. However, as the reaction progresses, molten materials continue to accumulate in the vicinity of the pores, ultimately resulting in closed or semi-closed structured pores. Simultaneously, both type A and type C discharges occur within pores, leading to the evolution of encompassing "honeycomb" structured pores within open pores.

Author Contributions: Conceptualization, G.L. (Guang Li), G.L. (Guodong Li) and Y.X.; investigation, G.L. (Guodong Li); project administration, G.L. (Guodong Li) and Y.X.; validation, G.L. (Guodong Li), G.L. (Guang Li) and Y.X.; visualization, G.L. (Guodong Li); writing—original draft, G.L. (Guodong Li); writing—review and editing, G.L. (Guodong Li). All authors have read and agreed to the published version of the manuscript.

Conflicts of Interest: The authors declare no conflict of interest.

References

1. Hegab, A.; Dahuwa, K.; Islam, R.; Cairns, A.; Khurana, A.; Shrestha, S.; Francis, R. Plasma electrolytic oxidation thermal barrier coating for reduced heat losses in IC engines. *Appl. Therm. Eng.* **2021**, *196*, 117316. [CrossRef]
2. Sobolev, A.; Peretz, T.; Borodianskiy, K. Fabrication and Characterization of Ceramic Coating on Al7075 Alloy by Plasma Electrolytic Oxidation in Molten Salt. *Coatings* **2020**, *10*, 993. [CrossRef]
3. Hussein, R.O.; Nie, X.; Northwood, D.O. Effect of current mode on the plasma discharge, microstructure and corrosion resistance of oxide coatings produced on 1100 aluminum alloy by plasma electrolytic oxidation. *WIT Trans. Eng. Sci.* **2019**, *124*, 3–16.
4. Zhao, C.; Wang, X.; Yu, B.; Cai, M.; Yu, Q.; Zhou, F. Research Progress on the Wear and Corrosion Resistant Plasma Electrolytic Oxidation Composite Coatings on Magnesium and Its Alloys. *Coatings* **2023**, *13*, 1189. [CrossRef]
5. Xiang, M.; Li, T.; Zhao, Y.; Chen, M. The Influence of Negative Voltage on Corrosion Behavior of Ceramic Coatings Prepared by MAO Treatment on Steel. *Coatings* **2022**, *12*, 710. [CrossRef]
6. Wang, S.; Zhou, L.; Li, C.; Li, Z.; Li, H.; Yang, L. Micrographic Properties of Composite Coatings Prepared on TA2 Substrate by Hot-Dipping in Al-Si Alloy and Using Micro-Arc Oxidation Technologies (MAO). *Coatings* **2020**, *10*, 374. [CrossRef]
7. Salahshouri, F.; Saebnoori, E.; Borghei, S.; Mossahebi-Mohammadi, M.; Bakhsheshi-Rad, H.R.; Berto, F. Plasma Electrolytic Oxidation (PEO) Coating on γ-TiAl Alloy: Investigation of Bioactivity and Corrosion Behavior in Simulated Body Fluid. *Metals* **2022**, *12*, 1866. [CrossRef]
8. Staszuk, M.; Reimann, A.; Pakuła, D.; Pawlyta, M.; Musztyfaga-Staszuk, M.; Czaja, P.; Beneš, P. Investigations of TiO_2/NanoTiO_2 Bimodal Coatings Obtained by a Hybrid PVD/ALD Method on Al-Si-Cu Alloy Substrate. *Coatings* **2022**, *12*, 338. [CrossRef]
9. Omar, N.I.; Yamada, M.; Yasui, T.; Fukumoto, M. Bonding Mechanism of Cold-Sprayed TiO_2 Coatings on Copper and Aluminum Substrates. *Coatings* **2021**, *11*, 1349. [CrossRef]
10. Hui, B.; Fu, X.; Gibson, D.; Child, D.; Song, S.; Fleming, L.; Rutins, G.; Chu, H.; Clark, C.; Reid, S. Automated Control of Plasma Ion-Assisted Electron Beam-Deposited TiO_2 Optical Thin Films. *Coatings* **2018**, *8*, 272. [CrossRef]
11. Nahum, E.Z.; Lugovskoy, S.; Lugovskoy, A.; Kazanski, B.; Sobolev, A. The study of hydroxyapatite growth kinetics on CP–Ti and Ti65Zr treated by Plasma electrolytic oxidation process. *J. Mater. Res. Technol.* **2023**, *24*, 2169–2186. [CrossRef]
12. Wu, Y.; Yang, Z.; Wang, R.; Wu, G.R.; Chen, D.; Wang, D.D.; Liu, X.T.; Li, D.L.; Guo, C.H.; Yu, S.X.; et al. An investigation of microstructure evolution for plasma electrolytic oxidation (PEO) coated Al in an alkaline silicate electrolyte. *Surf. Coat. Technol.* **2018**, *351*, 136–152. [CrossRef]
13. Wu, G.; Li, L.; Sun, M.; Wang, Y.; Luo, F.; Zhang, Q.; Liu, R.; Chen, Z.; Yao, J. Microstructural evolution and biological properties of PEO coating on SLM-prepared NiTi alloy. *Surf. Coat. Technol.* **2023**, *452*, 129065. [CrossRef]
14. Sobolev, A.; Peretz, T.; Borodianskiy, K. Synthesis and growth mechanism of ceramic coatings on an Al-Cu alloy using plasma electrolytic oxidation in molten salt. *J. Alloys Compd.* **2021**, *869*, 159309. [CrossRef]

15. Malinovschi, V.; Marin, A.; Andrei, V.; Coaca, E.; Mihailescu, C.N.; Lungu, C.P.; Radulescu, C.; Dulama, I.D. Obtaining and characterization of PEO layers prepared on CP-Ti in sodium dihydrogen phosphate dihydrate acidic electrolyte solution. *Surf. Coat. Technol.* **2019**, *375*, 621–636. [CrossRef]

16. Lee, J.; Jung, K.; Kim, S. Characterization of ceramic oxide coatings prepared by plasma electrolytic oxidation using pulsed direct current with different duty ratio and frequency. *Appl. Surf. Sci.* **2020**, *516*, 146049. [CrossRef]

17. Gao, F.; Hao, L.; Li, G.; Xia, Y. The plasma electrolytic oxidation micro-discharge channel model and its microstructure characteristic based on Ti tracer. *Appl. Surf. Sci.* **2018**, *431*, 13–16. [CrossRef]

18. Jovović, J.; Stojadinović, S.; Šišović, N.M.; Konjević, N. Spectroscopic characterization of plasma during electrolytic oxidation (PEO) of aluminium. *Surf. Coat. Technol.* **2011**, *206*, 24–28. [CrossRef]

19. Zhan, T.; Tu, W.; Cheng, Y.; Han, J.; Su, B.; Cheng, Y. The synthesis of micro and nano WO_3 powders under the sparks of plasma electrolytic oxidation of Al in a tungstate electrolyte. *Ceram. Int.* **2018**, *44*, 10402–10411. [CrossRef]

20. Stojadinović, S.; Vasilić, R.; Petković, M.; Kasalica, B.; Belča, I.; Žekić, A.; Zeković, L. Characterization of the plasma electrolytic oxidation of titanium in sodium metasilicate. *Appl. Surf. Sci.* **2013**, *265*, 226–233. [CrossRef]

21. Stojadinović, S.; Vasilić, R.; Petković, M.; Zeković, L. Plasma electrolytic oxidation of titanium in heteropolytungstate acids. *Surf. Coat. Technol.* **2011**, *206*, 575–581. [CrossRef]

22. Stojadinovic, S.; Vasilic, R.; Petkovic, M.; Belča, I.; Kasalica, B.; Perić, M.; Zeković, L. Luminescence during anodization of magnesium alloy AZ31. *Electrochim. Acta* **2012**, *59*, 354–359. [CrossRef]

23. Hussein, R.O.; Northwood, D.O.; Nie, X. The influence of pulse timing and current mode on the microstructure and corrosion behaviour of a plasma electrolytic oxidation (PEO) coated AM60B magnesium alloy. *J. Alloys Compd.* **2012**, *541*, 41–48. [CrossRef]

24. Hussein, R.O.; Nie, X.; Northwood, D.O. An investigation of ceramic coating growth mechanisms in plasma electrolytic oxidation (PEO) processing. *Electrochim. Acta* **2013**, *112*, 111–119. [CrossRef]

25. Liu, R.; Wu, J.; Xue, W.; Qu, Y.; Yang, C.; Wang, B.; Wu, X. Discharge behaviors during plasma electrolytic oxidation on aluminum alloy. *Mater. Chem. Phys.* **2014**, *148*, 284–292. [CrossRef]

26. Kasalica, B.; Petković-Benazzouz, M.; Sarvan, M.; Belča, I.; Maksimović, B.; Misailović, B.; Popović, Z. Mechanisms of plasma electrolytic oxidation of aluminum at the multi-hour timescales. *Surf. Coat. Technol.* **2020**, *390*, 125681. [CrossRef]

27. Li, G.; Ma, F.; Li, Z.; Xu, Y.; Gao, F.; Guo, L.; Zhu, J.; Li, G.; Xia, Y. Influence of Applied Frequency on Thermal Physical Properties of Coatings Prepared on Al and AlSi Alloys by Plasma Electrolytic Oxidation. *Coatings* **2021**, *11*, 1439. [CrossRef]

28. Hariprasad, S.; Varma, A.; Saikiran, A.; Arun, S.; Parfenov, E.V.; Rameshbabu, N. Influence of pulse frequency on the morphological and corrosion characteristics of the plasma electrolytic oxidized ZM21 magnesium alloy. *Mater. Today Proc.* **2021**, *39*, 1456–1464. [CrossRef]

29. Nikoomanzari, E.; Karbasi, M.; Melo, W.; Moris, H.; Babaei, K.; Giannakis, S.; Fattah-alhosseini, A. Impressive strides in antibacterial performance amelioration of Ti-based implants via plasma electrolytic oxidation (PEO): A review of the recent advancements. *Chem. Eng. J.* **2022**, *441*, 136003. [CrossRef]

30. Barati Darband, G.; Aliofkhazraei, M.; Hamghalam, P.; Valizade, N. Plasma electrolytic oxidation of magnesium and its alloys: Mechanism, properties and applications. *J. Magnes. Alloys* **2017**, *5*, 74–132. [CrossRef]

31. Sandhyarani, M.; Rameshbabu, N.; Venkateswarlu, K.; Sreekanth, D.; Subrahmanyam, C. Surface morphology, corrosion resistance and in vitro bioactivity of P containing ZrO_2 films formed on Zr by plasma electrolytic oxidation. *J. Alloys Compd.* **2013**, *553*, 324–332. [CrossRef]

32. Yang, X.; Chen, L.; Qu, Y.; Liu, R.; Wei, K.; Xue, W. Optical emission spectroscopy of plasma electrolytic oxidation process on 7075 aluminum alloy. *Surf. Coat. Technol.* **2017**, *324*, 18–25. [CrossRef]

33. Jovović, J.; Stojadinović, S.; Šišović, N.M.; Konjević, N. Spectroscopic study of plasma during electrolytic oxidation of magnesium- and aluminium-alloy. *J. Quant. Spectrosc. Radiat. Transf.* **2012**, *113*, 1928–1937. [CrossRef]

34. Ji, S.; Weng, Y.; Wu, Z.; Ma, Z.; Tian, X.; Fu, R.K.; Lin, H.; Wu, G.; Chu, P.K.; Pan, F. Excellent corrosion resistance of P and Fe modified micro-arc oxidation coating on Al alloy. *J. Alloys Compd.* **2017**, *710*, 452–459. [CrossRef]

35. Hashemzadeh, M.; Raeissi, K.; Ashrafizadeh, F.; Simchen, F.; Hakimizad, A.; Santamaria, M.; Lampke, T. The importance of type of Ti-based additives on the PEO process and properties of Al_2O_3-TiO_2 coating. *Surf. Interfaces* **2023**, *36*, 102523. [CrossRef]

36. Mashtalyar, D.V.; Imshinetskiy, I.M.; Nadaraia, K.V.; Gnedenkov, A.S.; Suchkov, S.N.; Opra, D.P.; Pustovalov, E.V.; Ustinov, A.Y.; Sinebryukhov, S.L.; Gnedenkov, S.V. Effect of TiO_2 nanoparticles on the photocatalytic properties of PEO coatings on Mg alloy. *J. Magnes. Alloys* **2023**, *11*, 735–752. [CrossRef]

37. Vargas-Villanueva, S.; Torres-Ceron, D.A.; Amaya-Roncancio, S.; Arellano-Ramírez, I.D.; Riva, J.S.; Restrepo-Parra, E. Study of the incorporation of S in $TiO_2/SO4^{2-}$ Coatings produced by PEO process through XPS and DFT. *Appl. Surf. Sci.* **2022**, *599*, 153811. [CrossRef]